Development of high-temperature ferromagnetism in SnO_2 and paramagnetism in SnO by Fe doping

A. Punnoose,[1,*] J. Hays,[1] A. Thurber,[1] M. H. Engelhard,[2] R. K. Kukkadapu,[2] C. Wang,[2] V. Shutthanandan,[2] and S. Thevuthasan[2]

[1]*Department of Physics, Boise State University, Boise, Idaho 83725-1570, USA*

[2]*Environmental Molecular Sciences Laboratory, Pacific Northwest National Laboratory, Richland, Washington 99352, USA*

(Received 26 May 2005; published 2 August 2005)

We report the development of room-temperature ferromagnetism in chemically synthesized powder samples of $Sn_{1-x}Fe_xO_2$ ($0.005 \leqslant x \leqslant 0.05$) and paramagnetic behavior in an identically synthesized set of $Sn_{1-x}Fe_xO$. The ferromagnetic $Sn_{0.99}Fe_{0.01}O_2$ showed a Curie temperature $T_C = 850$ K, which is among the highest reported for transition-metal-doped semiconductor oxides. With increasing Fe doping, the lattice parameters of SnO_2 decreased and the saturation magnetization increased, suggesting a strong structure-magnetic property relationship. When the $Sn_{0.95}Fe_{0.05}O_2$ was prepared at different temperatures between 200 and 900 °C, systematic changes in the magnetic properties were observed. Combined Mössbauer spectroscopy and magnetometry measurements showed a ferromagnetic behavior in $Sn_{0.95}Fe_{0.05}O_2$ samples prepared at and above 350 °C, but the ferromagnetic component decreased gradually as preparation temperature approached 600 °C. All $Sn_{0.95}Fe_{0.05}O_2$ samples prepared above 600 °C were paramagnetic. X-ray photoelectron spectroscopy, magnetometry, and particle induced x-ray emission studies showed that the Fe dopants diffuse towards the surface of the particles in samples prepared at higher temperatures, gradually destroying the ferromagnetism. Mössbauer studies showed that the magnetically ordered Fe^{3+} spins observed in the $Sn_{0.95}Fe_{0.05}O_2$ sample prepared at 350 °C is only ~24% of the uniformly incorporated Fe^{3+}. No evidence of any iron oxide impurity phases were detected in $Sn_{1-x}Fe_xO_2$ or $Sn_{1-x}Fe_xO$, suggesting that the emerging magnetic interactions in these systems are most likely related to the properties of the host systems SnO_2 and SnO, and their oxygen stoichiometry.

DOI: 10.1103/PhysRevB.72.054402 PACS number(s): 75.50.Pp, 72.25.−b, 73.63.Bd

I. INTRODUCTION

Development of room-temperature ferromagnetism (RTFM) in conventional semiconductors is currently attracting intense interest due to their potential use in spintronics applications.[1,2] Unfortunately, most traditional transition-metal-doped magnetic semiconductor systems only exhibit ferromagnetism well below room temperature.[3] Recently, new candidates for RTFM have been predicted theoretically, most of which propose hole-mediated exchange as a stronger interaction than electron-mediated exchange.[4] However, recent experimental reports indicate ferromagnetism in *n*-type semiconductor oxides such as $Ti_{1-x}Co_xO_2$ (see Ref. 5) and $Sn_{1-x}Co_xO_2$.[6,7] Ogale *et al.*[6] investigated pulsed-laser-deposited thin films of $Sn_{1-x}Co_xO_2$ ($x < 0.3$) and found strong ferromagnetic behavior at room temperature with a giant magnetic moment of $7.5 \pm 0.5\ \mu_B$/Co. In a recent paper,[7] Coey *et al.* observed RTFM in $Sn_{1-x}Fe_xO_2$ thin films grown by pulsed-laser deposition with $x = 0.05$, but with a low magnetic moment of $1.8\ \mu_B$/Fe ion. In this work, we have undertaken a search for RTFM in chemically synthesized powder samples of *p*-type SnO and *n*-type SnO_2 (see Ref. 8) by doping them with Fe. Our powder samples of $Sn_{1-x}Fe_xO_2$ with $x \leqslant 0.05$ showed RTFM, whereas only paramagnetic behavior was observed in $Sn_{1-x}Fe_xO$. Investigation of the samples prepared with different Fe concentrations and at different preparation temperatures suggest that the ferromagnetic/paramagnetic behavior is due to the incorporation of Fe ions into the host lattices. Details of these studies follow.

II. EXPERIMENTAL DETAILS

Appropriate amounts of $SnCl_2$ (99% min.), $FeCl_2$ (99.5%), and NH_4OH were added to de-ionized water to produce solutions with molarities of 1, 0.02, and 5M, respectively. All the samples were prepared by reacting the 0.02M $FeCl_2$ and 1M $SnCl_2$ solutions at 80 °C {molar ratio of $x = [Fe]/([Fe]+[Sn])$} with a large amount (~1.5 times precursor solution volume) of a 5M solution of NH_4OH. The resulting precipitate was washed to remove any water-soluble byproducts and annealed in air for 3 h at 200 and 600 °C to obtain $Sn_{1-x}Fe_xO$ and $Sn_{1-x}Fe_xO_2$, respectively. To obtain more insight into possible Fe impurity phases that might form under these synthesis conditions, pure iron oxide samples were also prepared following identical synthesis procedures without using any $SnCl_2$. Several samples of $Sn_{0.95}Fe_{0.05}O_2$ were prepared by annealing the same precipitate at temperatures of 350, 450, 600, 750, and 900 °C to investigate the effect of preparation temperature.

The nominal Fe doping concentrations were confirmed by particle-induced x-ray emission (PIXE) measurements carried out in the accelerator facility at Pacific Northwest National Laboratory. The powder samples were first mixed with a very small amount of polyvinyl alcohol and then pelletized using a hand-held press. The samples were then irradiated with a 2.0 MeV He^+ ion beam and the x rays emitted during the de-excitation process within the atoms were analyzed using an x-ray spectrometer.

X-ray diffraction (XRD) spectra were recorded at room temperature on a Phillips X'Pert x-ray diffractometer with a

Cu K_α source ($\lambda = 1.5418$ Å) in Bragg-Brentano geometry. The loose powder samples were leveled in the sample holder to ensure a smooth surface and mounted on a fixed horizontal sample plane. Data analyses were carried out using profile fits of selected individual XRD peaks. High-resolution transmission electron microscopy (TEM) analysis was carried out on a JEOL JEM 2010 microscope with a specified point-to-point resolution of 0.194 nm. The operating voltage of the microscope was 200 kV. All images were digitally recorded with a slow scan CCD camera (image size 1024×1024 pixels), and image processing was carried out using the Digital Micrograph software from Gatan (Pleasant, California, USA). Energy dispersive x-ray spectroscopy (EDX) was carried out using the Oxford Link system attached to the TEM.

For Mössbauer spectroscopy measurements, randomly oriented absorbers were prepared by mixing approximately 30 mg of sample with petroleum jelly in a 0.375 in. thick and 0.5 in. internal diameter Cu holder sealed at one end with clear tape. The holder was entirely filled with the sample mixture and sealed at the other end with tape. Spectra were collected using a 50 mCi (initial strength) ^{57}Co/Rh source. The velocity transducer MVT-1000 (WissEL) was operated in constant acceleration mode (23 Hz, ±12 mm/s). An Ar-Kr proportional counter was used to detect the radiation transmitted through the holder, and the counts were stored in a multichannel scalar as a function of energy (transducer velocity) using a 1024 channel analyzer. Data were folded to 512 channels to give a flat background and a zero-velocity position corresponding to the center shift (CS or δ) of a metallic iron foil at room temperature. Calibration spectra were obtained with a 20 μm thick α-Fe(m) foil (Amersham, England) placed in exactly the same position as the samples to minimize any errors due to changes in geometry. Sample thickness corrections were not carried out. The data were modeled with RECOIL software (University of Ottawa, Canada) using a Voigt-based spectral fitting routine.[9]

X-ray photoelectron spectroscopy (XPS) measurements were performed on powder samples using a Physical Electronics Quantum 2000 Scanning ESCA Microprobe. This system uses a focused monochromatic Al K_α x-ray (1486.7 eV) source and a spherical section analyzer. The instrument has a 16 element multichannel detector. The x-ray beam used was a 105 W, 100 μm diameter beam that was rastered over a 1.4 mm $\times$ 0.2 mm rectangle on the sample. The powder samples were mounted using a small amount of double-coated carbon conductive tape. The x-ray beam was incident normal to the sample and the photoelectron detector was at 45° off-normal. Data was collected using a pass energy of 46.95 eV. For the Ag $3d_{5/2}$ line, these conditions produce full width at half-maximum of better than 0.98 eV. Although the binding energy (BE) scale was calibrated using the Cu $2p_{3/2}$ feature at 932.62±0.05 eV and Au $4f$ feature at 83.96±0.05 eV for known standards, the Fe-doped SnO_2 surface experienced variable degrees of charging. Low-energy electrons at ~1 eV, 21 μA, and low-energy Ar^+ ions were used to minimize this charging. The BE positions were referenced using the 486.7 eV position for the Sn $3d_{5/2}$ feature for the $Sn_{1-x}Fe_xO_2$ samples and the 486.9 eV position for the $Sn_{1-x}Fe_xO$ samples. XPS spectra were also collected after Ar^+ ion sputtering using a 4 kV Ar^+ ion beam rastered over a 4 mm $\times$ 4 mm sample area. The sputter rates were calibrated using a SiO_2 standard with known thickness.

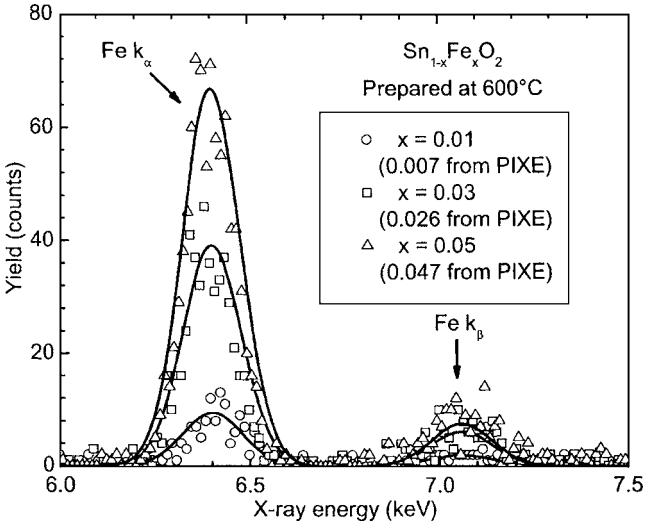

FIG. 1. Typical PIXE spectra from the $Sn_{1-x}Fe_xO_2$ samples showing the Fe region. Fe concentrations (x) obtained by PIXE data simulation (solid lines) are given in parentheses.

Magnetic measurements were carried out as a function of temperature (4 to 350 K) and magnetic field (0 to±65 kOe) using a commercial magnetometer (Quantum Design, PPMS) equipped with a superconducting magnet. Measurements were carried out on tightly packed powder samples placed in a clear plastic drinking straw. The data reported here were corrected for the background signal from the sample holder (clear plastic drinking straw) with diamagnetic susceptibility $\chi = -4.1 \times 10^{-8}$ emu/Oe.

III. EXPERIMENTAL RESULTS AND ANALYSIS

A. Particle-induced x-ray emission studies

The Fe concentrations of the $Sn_{1-x}Fe_xO$ and $Sn_{1-x}Fe_xO_2$ samples were determined using particle-induced x-ray emission measurements. The PIXE data obtained from selected samples are shown in Fig. 1. The Fe concentrations shown in Table I, estimated by simulating the experimental PIXE spectra after removing the background due to bremsstrahlung, are in reasonable agreement with their nominal concentrations.

B. X-ray diffraction studies

XRD patterns of powder $Sn_{1-x}Fe_xO$ samples [Fig. 2(a)] showed strong peaks of tetragonal SnO with some weak SnO_2 traces. The lattice parameters a and c, determined using the (101) and (110) peaks, showed an increase with x, as shown in Fig. 3(a). The experimentally determined lattice parameters of the pure SnO samples are lower than that reported for pure synthetic bulk romarchite and this may be due to changes in the oxygen stoichiometry and/or particle size effect. The $Sn_{1-x}Fe_xO_2$ samples showed strong XRD peaks due to the cassiterite phase of SnO_2, with much weaker peaks of the metastable orthorhombic SnO_2 phase.[10]

TABLE I. Atomic concentration estimates of $Sn_{1-x}Fe_xO$ and $Sn_{1-x}Fe_xO_2$ obtained from PIXE and XPS measurements.

Nominal Fe%	Fe% from PIXE	Preparation temperature (°C)	Major XRD identified phase	Processing conditions	Estimated atomic % from XPS		
					Fe	Sn	O
0	···	200	$Sn_{1-x}Fe_xO$	As-prepared	···	29.2	55.4
1	0.79	200	$Sn_{1-x}Fe_xO$	As-prepared	···	30.1	61.0
3	3.07	200	$Sn_{1-x}Fe_xO$	As-prepared	···	···	···
5	4.54	200	$Sn_{1-x}Fe_xO$	As-prepared	1.2	29.2	61.0
0	···	600	$Sn_{1-x}Fe_xO_2$	As-prepared	···	31.2	61.2
1	0.66	600	$Sn_{1-x}Fe_xO_2$	As-prepared	···	31.7	62.2
3	2.66	600	$Sn_{1-x}Fe_xO_2$	As-prepared	···	···	···
5	4.89	600	$Sn_{1-x}Fe_xO_2$	As-prepared	3.1	27.7	59.7
5	···	350	$Sn_{1-x}Fe_xO_2$	As-prepared	0.7	30.0	60.2
5	···	450	$Sn_{1-x}Fe_xO_2$	As-prepared	1.1	31.8	64.2
5	···	750	$Sn_{1-x}Fe_xO_2$	As-prepared	3.9	28.6	62.3
5	4.00	900	$Sn_{1-x}Fe_xO_2$	As-prepared	6.2	23.1	56.3
5	···	900	$Sn_{1-x}Fe_xO_2$	10 nm Ar^+ ion sputtered	4.5	36.3	57.5
5	···	900	$Sn_{1-x}Fe_xO_2$	20 nm Ar^+ ion sputtered	3.4	39.7	56.2

The peak intensities, positions, and widths of the XRD lines changed with x in $Sn_{1-x}Fe_xO_2$, as illustrated in Fig. 2(b). Lattice parameters a and c and the particle size L (see Ref. 11) [Figs. 3(b) and 3(c)], estimated using the cassiterite (110) and (202) peaks of the nanoscale samples of $Sn_{1-x}Fe_xO_2$, decreased as x increased from 0.005 to 0.05. The directly opposite changes in the lattice parameters observed in $Sn_{1-x}Fe_xO$ and $Sn_{1-x}Fe_xO_2$ with Fe doping concentration might reflect the effect of substituting Fe^{3+} for Sn^{4+} ions in SnO_2 and for Sn^{2+} ions in SnO. This might require rearrangement of neighboring oxygen ions for charge neutrality. When the 5% Fe-doped samples were prepared at different temperatures in the 200 to 900 °C range, the tetragonal SnO phase was observed at 200 °C and showed a gradual conversion to the SnO_2 phase with increasing preparation temperature until its apparent disappearance at $\geqslant$450 °C, as illustrated in Fig. 4(a). The lattice parameter a and the unit cell volume V decreased and the lattice parameter c increased with increasing preparation temperature in the 350 to 600 °C range, as shown in Fig. 4(b). Above 600 °C, these trends were reversed, and the lattice volume approached closer to the pure SnO_2 range.

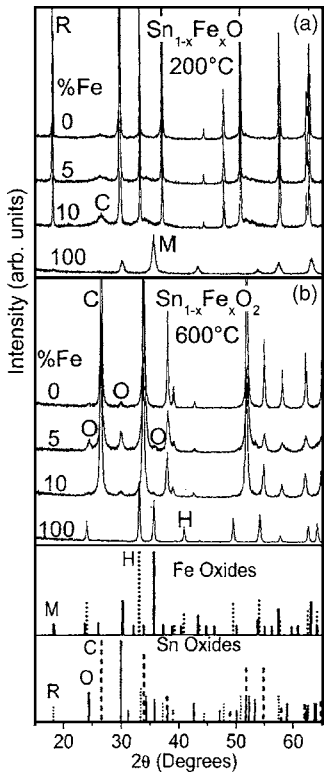

FIG. 2. Panels (a) and (b) show XRD patterns of $Sn_{1-x}Fe_xO$ (prepared at 200 °C) and $Sn_{1-x}Fe_xO_2$ (prepared at 600 °C), respectively, along with reference lines of orthorhombic SnO_2 (solid lines, marked "O"), romarchite SnO (dotted lines, marked "R") cassiterite SnO_2 (dashed lines, marked "C") phases, hematite (marked "H"), and maghemite (marked "M") phases of Fe_2O_3.

The pure iron oxide sample (prepared under identical synthesis conditions, but with no $SnCl_2$) showed maghemite [γ-Fe_2O_3, Fig. 2(a)] and hematite [α-Fe_2O_3, Fig. 2(b)] phases,[12] with average particle sizes of 22 and 53 nm at 200 and 600 °C preparations, respectively. No trace of iron metal, oxides, or any binary tin-iron phases were observed in any of the doped samples with $x \leqslant 0.10$. This is consistent with the reported solubility limit of up to 10% Fe in SnO_2.[10,13] This along with the fact that the x-ray diffractometer employed can only detect phases that are $\geqslant$1.5%, experimental data collected from samples with $x \leqslant 0.05$ only are included in the investigations reported here.

C. Transmission electron microscopy studies

Transmission electron microscopy measurements showed significant changes in the shape and size of the $Sn_{1-x}Fe_xO_2$

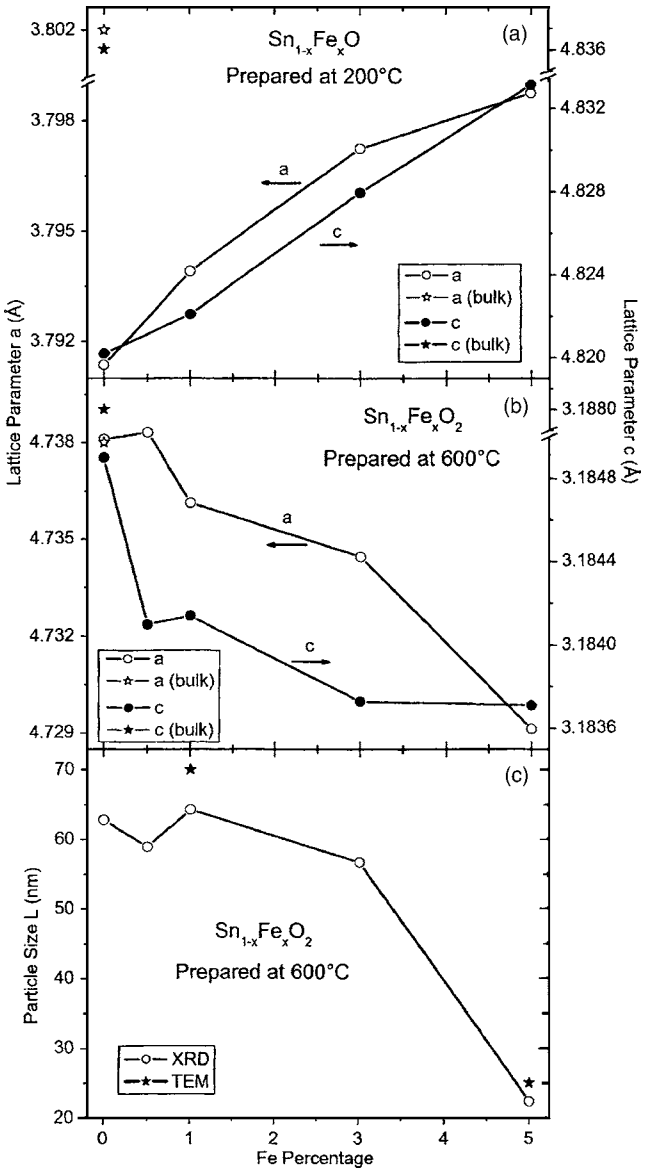

FIG. 3. (a) Changes in the lattice parameters a and c of tetragonal SnO calculated using (101) and (110) peaks as a function of Fe percentage. (b) Changes in the lattice parameters a and c of cassiterite SnO_2 calculated using the (110) and (202) peaks as a function of Fe percentage. (c) Particle size of $Sn_{1-x}Fe_xO_2$ as a function of x calculated from the tetragonal cassiterite XRD peak (110). The particle sizes determined from TEM are marked with stars in (c). The reported magnitudes of the lattice parameters of bulk SnO and SnO_2 are also shown in (a) and (b).

particles with different Fe doping concentrations, as shown in Figs. 5(a) and 5(b). These particles were all elongated with their aspect ratios and average L changing from ~1.25 and 70 nm, respectively, for $x=0.01$ to 1.7 and 25 nm for $x=0.05$. The crystallite sizes match very well with similar estimates obtained from the XRD data [see Fig. 3(c)]. The energy dispersive x-ray spectroscopy measurements carried out on 1 and 5% Fe-doped SnO_2 samples showed Fe concentrations in reasonable agreement with the estimates obtained from PIXE studies. The TEM images of the $Sn_{1-x}Fe_xO$ samples showed the presence of large micron-sized particles

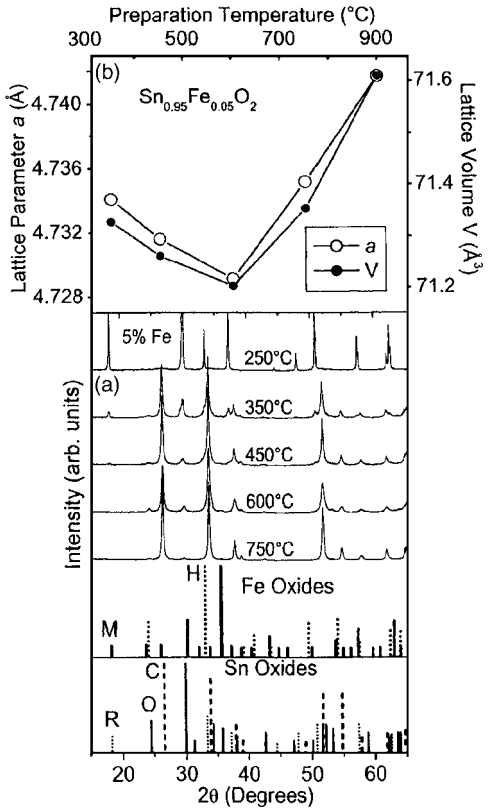

FIG. 4. (a) XRD patterns of 5% Fe-doped samples prepared by annealing the reaction precipitate at different temperatures shown above, along with reference lines of orthorhombic SnO_2 (solid lines, marked "O"), romarchite SnO (dotted lines, marked "R") cassiterite SnO_2 (dashed lines, marked "C") phases, hematite (marked "H") and maghemite (marked "M") phases of Fe_2O_3. (b) Changes in the lattice parameter a and the lattice volume of cassiterite $Sn_{0.95}Fe_{0.05}O_2$ as a function of preparation temperature. The change in the lattice parameter c was minimal.

with a different shape, as shown in Fig. 5(c).

Two samples of $Sn_{0.95}Fe_{0.05}O_2$ prepared at 350 and 900 °C were carefully investigated using TEM, selected area electron diffraction, and EDX studies. TEM data, shown in Figs. 6(a) and 6(b), clearly showed sintering effects and an increase in the particle size as the preparation temperature increased from 350 to 900 °C. Electron diffraction patterns taken from several particles confirmed the SnO_2 structure in both samples and no evidence for iron oxides or other impurity phases were observed.

D. Mössbauer spectroscopy measurements

Three selected samples were investigated using Mössbauer spectroscopy, and their spectra are shown in Fig. 7. The $Sn_{0.95}Fe_{0.05}O$ sample prepared at 200 °C showed [Fig. 7(a)] a well-defined doublet, suggesting that the incorporated Fe is paramagnetic and in the 3+ oxidation state in an octahedral environment. No evidence of any Fe^{2+} ions was detected in this sample.

Experimental and fit-derived room-temperature (RT) Mössbauer spectra of the $Sn_{0.95}Fe_{0.05}O_2$ sample prepared at

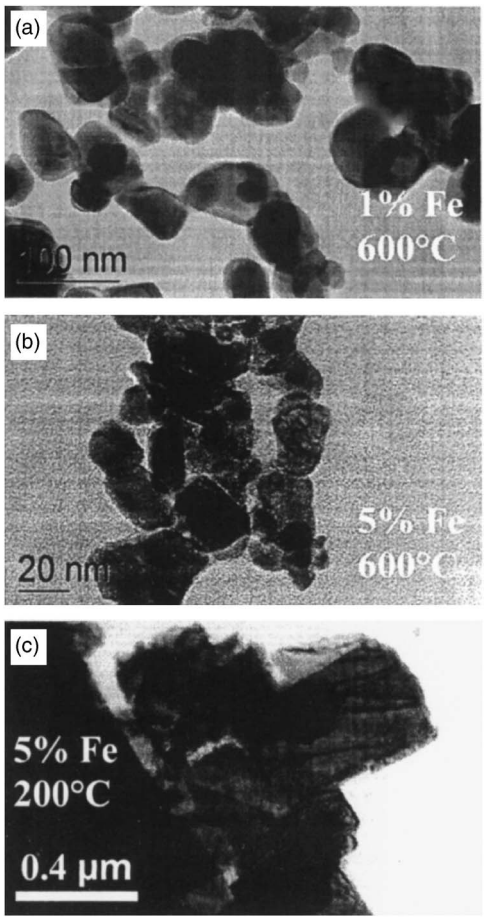

FIG. 5. Panels (a) and (b) show TEM images of $Sn_{1-x}Fe_xO_2$ prepared at 600 °C with $x=0.01$ and 0.05, respectively. Panel (c) shows the TEM image of $Sn_{1-x}Fe_xO$ prepared at 200 °C with $x=0.05$.

350 °C are shown in Fig. 7(b). The spectrum displayed a well-defined sextet (magnetic component; 24% spectral area) and a central doublet (paramagnetic component; 76% spectral area). The fit-derived parameters of the Fe sextet are center shift $\delta=0.38$ mm/s, quadrupole shift parameter $\varepsilon=-0.1$ mm/s, and hyperfine magnetic field $B_{hf}=50.3$ T, whereas the parameters of the doublet are $\delta=0.37$ mm/s and quadrupole shift $\varepsilon=0.85$ mm/s.

It is evident from the fit-derived Mössbauer parameters that the sextet feature (magnetic component of the sample) in Fig. 7(b) is not due to crystalline bulk Fe oxides such as magnetite, hematite, goethite, or maghemite.[14–16] Magnetite, a mixed oxide of Fe^{2+} and Fe^{3+}, displays two well-defined sextets in its RT Mössbauer spectrum.[14] This is due to the presence of Fe in both tetrahedral (Fe^{3+}) and octahedral sites (Fe^{2+} and Fe^{3+} at 1:1 ratio displays a sextet peak due to $Fe^{2.5+}$ because of Verwey transition): *A* and *B* sites of the inverse spinel structure. Hematite, on the other hand, displays a well-defined sextet with $B_{hf}=51.8$ T, $\delta=0.37$ mm/s and $\varepsilon=-0.20$ mm/s,[16] which is not the case here. Goethite displays a well-defined sextet with $B_{hf}=38$ T, $\delta=0.37$ mm/s, and $\varepsilon=-0.26$ mm/s.[16] It also appears from the derived Mössbauer parameters that the sextet feature in Fig. 7(b) is unlikely due to maghemite. The derived parameters are different from those of synthetic pure maghemite with $\delta=0.23-0.35$ mm/s, $\varepsilon=0.02$ mm/s, and $B_{hf}=50$ T.[16] The experimental conditions employed to synthesize the binary oxides in this study also imply nonformation of maghemite.[12]

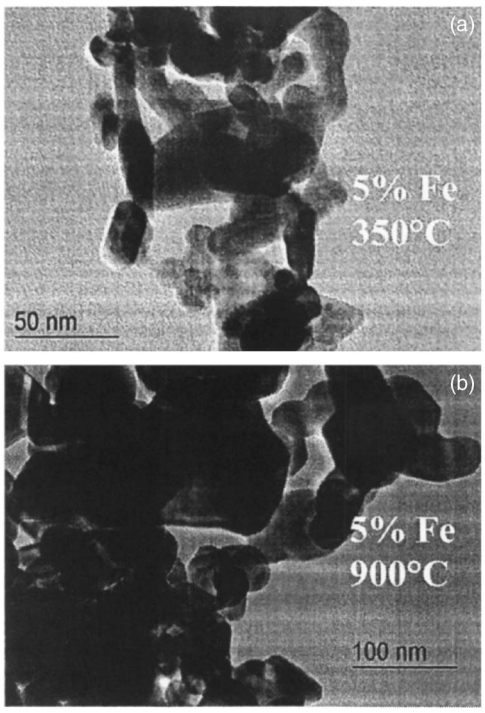

FIG. 6. Panels (a) and (b) show TEM images of $Sn_{0.95}Fe_{0.05}O_2$ prepared at 350 and 900 °C respectively.

The derived Mössbauer parameters of the central doublet, which is due to contribution from paramagnetic Fe site(s) to the sample, are not in favor of the formation of small particle magnetite and goethite. Small-particle Fe oxides such as magnetite (<10 nm),[14] goethite (<15 nm),[15] and hematite (<8 nm) (see Ref. 15) display a doublet at RT (well below their magnetic ordering temperature) due to superparamagnetism. The parameters of the doublet in Fig. 7(b), however, are inconsistent with superparamagnetic iron oxides.[14–17] The derived Mössbauer parameters of magnetite and hematite are $\delta=0.22$ mm/s and $\varepsilon=0$ to 0.6 mm/s, and $\delta=0.35$ mm/s and $\varepsilon=0.49$ mm/s, respectively, while the quadrupole splitting of goethite is around $\varepsilon=0.48$ mm/s. Moreover, any such iron oxides, if present in the superparamagnetic nanoparticle form, cannot produce the hysteresis loops with a finite coercivity (~60 Oe) observed in the magnetic studies (see Sec. III F). This observation along with the nonformation of "large" particle magnetite, hematite, and goethite (as mentioned above) in the sample implies absence of conditions that dictate their formation.

Thus, the Mössbauer data, shown in Fig. 7(b), suggests that the sextet results from magnetically ordered Fe^{3+}, which constitutes 24% of the incorporated Fe ions. This is in excellent agreement with a similar estimate of Coey *et al.*[7] on pulsed-laser-deposited thin film samples of $Sn_{0.95}Fe_{0.05}O_2$ in which they found 23% Fe in the magnetically ordered state. Interestingly, the Mössbauer data of the same $Sn_{0.95}Fe_{0.05}O_2$

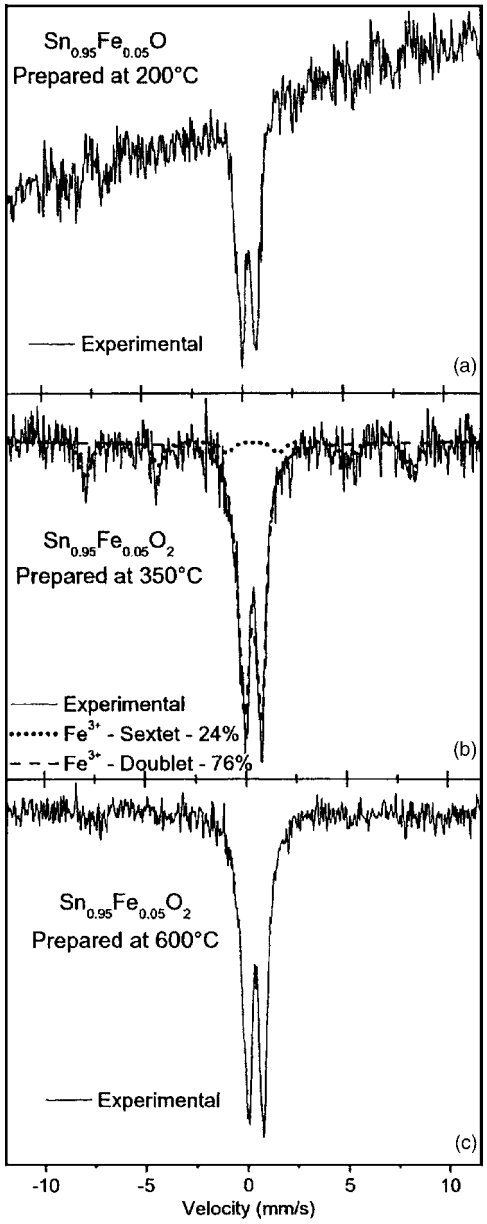

FIG. 7. Panel (a) shows the room-temperature Mössbauer spectra of $Sn_{0.95}Fe_{0.05}O$. Panels (b) and (c) show the room-temperature Mössbauer spectra of $Sn_{0.95}Fe_{0.05}O_2$ prepared at 350 and 600 °C, respectively.

powder prepared by annealing the precipitate at 600 °C [see Fig. 7(c)] showed mainly a doublet structure (corresponding to paramagnetic Fe^{3+}) with very weak traces of the sextet lines. This clearly suggests that the ferromagnetically ordered Fe^{3+} spins are converted to a paramagnetic spin system as the preparation temperature increased from 350 to 600 °C.

E. X-ray photoelectron spectroscopy studies

The Fe $3p_{1/2}$ XPS spectral region of $Sn_{1-x}Fe_xO_2$ (prepared by annealing the precipitate at 600 °C) samples with $x=0.01$ and 0.05 are shown in Fig. 8. Similar data obtained from hematite and maghemite phases of pure Fe_2O_3 prepared

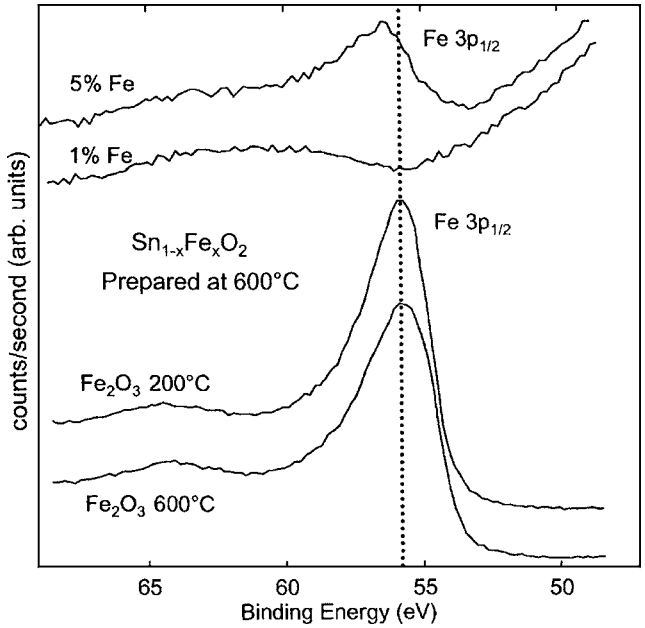

FIG. 8. XPS spectra of $Sn_{1-x}Fe_xO_2$ prepared at 600 °C with different values of x as indicated. Reference data obtained from maghemite and hematite forms of Fe_2O_3 prepared under identical synthesis conditions (but with no Sn precursors) are also shown.

under identical conditions are also shown for comparison. The XPS peaks are not clearly visible in the 1% Fe-doped samples; however, clear peaks were observed in $Sn_{0.95}Fe_{0.05}O_2$. This discrepancy may be related to the limited Fe detection ability of the XPS system. The XPS peaks of both hematite and maghemite phases occur at ~55.7 eV, which matches well with literature reports.[18] However, the core level peak of Fe in $Sn_{1-x}Fe_xO_2$ (Fig. 8) and $Sn_{1-x}Fe_xO$ (Fig. 9, 200 °C data) showed a slight shift to higher binding energies (~56.5 eV) compared to the Fe oxides, indicating the difference in the atomic environment surrounding the incorporated Fe ions. McIntyre and Zetaruk[18] have reported an Fe $3p_{1/2}$ binding energy of 53.9 eV for the magnetite (Fe_3O_4) form of iron oxide. Thus, the XPS data clearly suggest that the Fe peaks observed from the $Sn_{1-x}Fe_xO_2$ and $Sn_{1-x}Fe_xO$ samples are not arising from any maghemite, hematite, or magnetite inclusions in the samples. The relative peak positions of the Sn and O peaks in the samples did not show any measurable change with Fe concentration, suggesting that their chemical environments do not change significantly. Atomic percentages of Sn, Fe, and O calculated using the Sn $3d_{5/2}$, Fe $3p_{1/2}$, and O $1s$ peaks are given in Table I.

Figure 9 shows the XPS data obtained from the $Sn_{0.95}Fe_{0.05}O$ and $Sn_{0.95}Fe_{0.05}O_2$ samples prepared by annealing the same reaction precipitate at 200, 350, 450, 600, 750, and 900 °C. In all these samples, the core level Fe peak was observed at ~56.5 eV and no measurable shifts towards the binding energies expected for magnetite (53.9 eV), hematite (55.7 eV) and maghemite (55.7 eV) were observed when the preparation temperature varied in the 350 to 900 °C range. Although the Fe doping concentration was 5%, the Fe XPS peaks systematically intensified with increasing preparation temperature. Atomic percentages of Sn, Fe, and O calculated

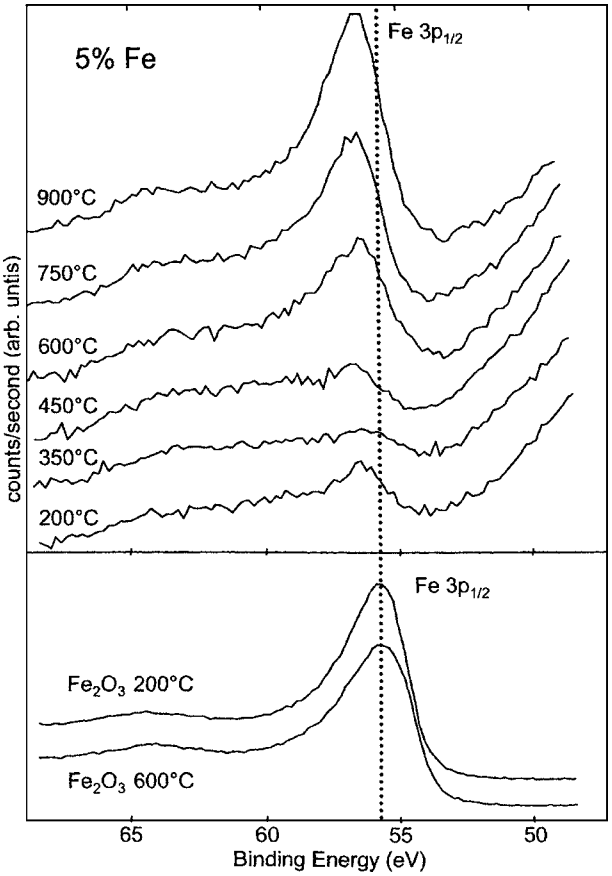

FIG. 9. Plot showing the XPS spectra of 5% Fe-doped samples as a function of the annealing temperature. Reference data obtained from maghemite and hematite forms of Fe_2O_3 prepared at 200 and 600 °C, respectively, under identical synthesis conditions (but with no Sn precursors) are also shown.

using the XPS peaks as a function of preparation temperature are given in Table I. Notwithstanding the difference between the atomic concentrations obtained from PIXE and XPS, the XPS estimates from $Sn_{0.95}Fe_{0.05}O_2$ showed a systematic increase in the Fe concentration from 0.7% to 6.2% as the annealing temperature increased from 350 to 900 °C. As mentioned above, the lower Fe estimates from the XPS data may be due to the relatively lower detectability of Fe using XPS. In the PIXE measurements discussed before, the Fe concentration of the $Sn_{0.95}Fe_{0.05}O_2$ samples prepared in the entire temperature range was always between 4% and 4.88% and no such systematic variation with preparation temperature was observed. Compared to PIXE, which is responsive to the entire bulk of the sample, XPS is a surface-sensitive technique. Therefore, the increasing differences between the Fe concentrations obtained from these two techniques clearly suggest a gradual and systematic surface diffusion of the doped Fe ions with increasing preparation temperature. This suggests that the $Sn_{0.95}Fe_{0.05}O_2$ samples prepared at lower temperatures produce a more uniform distribution of Fe in the entire crystallite. On the other hand, samples prepared at higher temperatures showed significant diffusion of the incorporated Fe ions towards the particle surface as preparation temperature increases to 900 °C.

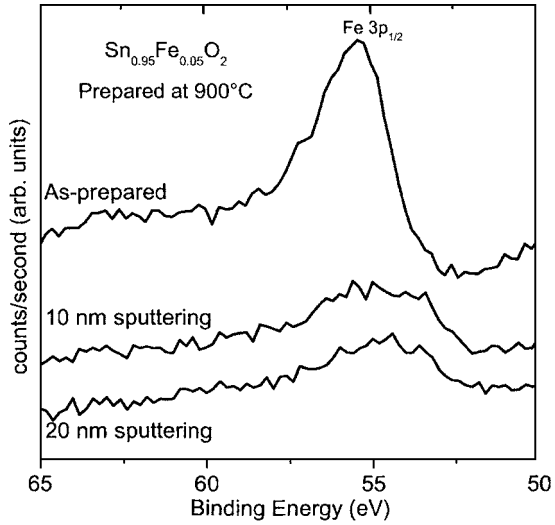

FIG. 10. Plot showing the XPS spectra of $Sn_{0.95}Fe_{0.05}O_2$ prepared at 900 °C along with that obtained from the same sample after removing 10 and 20 nm of surface layer by Ar^+ ion sputtering.

To further confirm the Fe surface diffusion possibility, XPS spectra were collected from the 900 °C prepared $Sn_{0.95}Fe_{0.05}O_2$ sample employing Ar^+ ion sputtering to remove surface layers from the powder samples mounted on carbon conductive tape (shown in Fig. 10). These measurements showed a gradual decrease in the Fe concentration from 6.23% in the as-prepared sample to 3.43% when a 20 nm surface layer is removed by Ar^+ ion sputtering (see Table I). This fully supports the above conclusion that the higher XPS estimates of Fe concentration obtained from $Sn_{0.95}Fe_{0.05}O_2$ samples prepared at higher temperatures ($\geqslant$600 °C) are indeed due to Fe surface diffusion. The observed dependence of the dopant diffusion effects on the preparation temperature is in reasonable agreement with similar studies conducted recently in Cu- and Fe-doped SnO_2 by Davis *et al.*[19] They have reported that the surface diffusion of the transition-metal dopants in SnO_2 starts at preparation temperatures of 400 °C. They have also observed a significant role of the dopants in inhibiting the grain growth, as observed in our XRD and TEM data shown in Fig. 3(c).

F. Magnetic measurements

1. $Sn_{1-x}Fe_xO$—*concentration dependence*

In Fig. 11(a), magnetization M of the $Sn_{1-x}Fe_xO$ samples measured at 5 K is shown as a function of magnetic field H along with their theoretical estimates obtained using the modified Brillouin-function-based form[20] for a paramagnetic system, given by

$$M = M_0\left\{\left(\frac{2J+1}{2J}\right)\coth\left[\frac{(2J+1)y}{2J}\right] - \left(\frac{1}{2J}\right)\coth\left(\frac{y}{2J}\right)\right\}, \tag{1}$$

where $y = g\mu_B JH/k(T+T_0)$, M_0 is the saturation magnetization, $g=2.0023$ is the spectroscopic splitting factor, μ_B is the Bohr magneton, and k is the Boltzmann constant. Based on

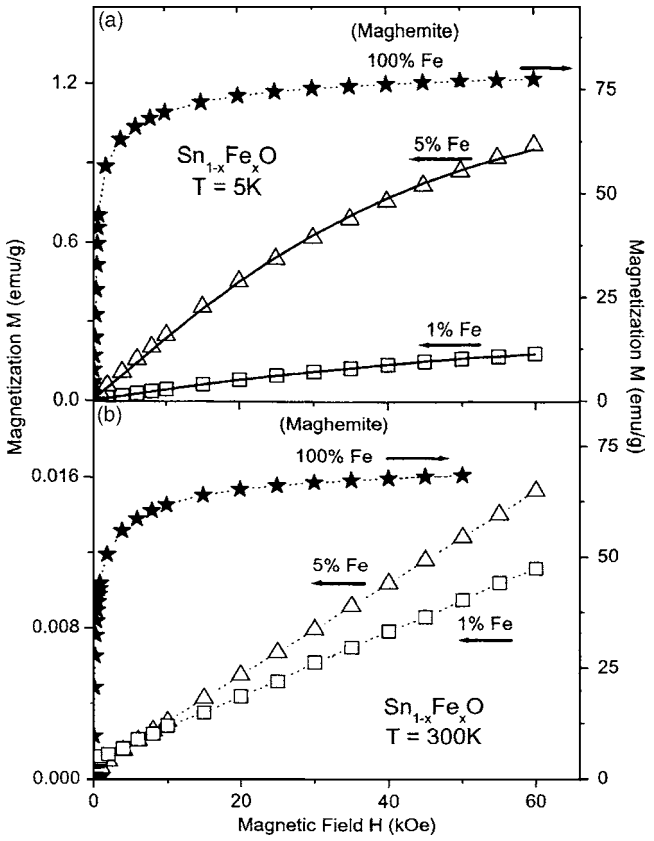

FIG. 11. (a) and (b) show M vs H data for $Sn_{1-x}Fe_xO$ samples measured at 5 and 300 K, respectively. Similar M vs H data collected from pure iron oxide (maghemite) prepared under identical conditions (but with no Sn precursors) are also shown. Solid lines through the data points are theoretical fits using Eq. (1).

the Mössbauer data discussed before, this analysis was carried out assuming $J=5/2$ (expected for Fe^{3+}). Here, T_0 is included as a measure of the magnetic interaction between the Fe spins, which prevents complete alignment of the spins even at the highest magnetic fields employed.[20] A larger T_0 indicates stronger antiferromagnetic (AF) interactions between the disordered Fe spins. Magnitudes of M_0 and T_0 obtained from this analysis are shown in Table II. M versus H plots of $Sn_{1-x}Fe_xO$ samples measured at 300 K showed a linear variation owing to the paramagnetic behavior, as shown in Fig. 11(b).

Magnetization M of the $Sn_{1-x}Fe_xO$ samples measured as a function of temperature T at a constant field $H=500$ Oe also showed the expected paramagnetic behavior (see Fig. 12)

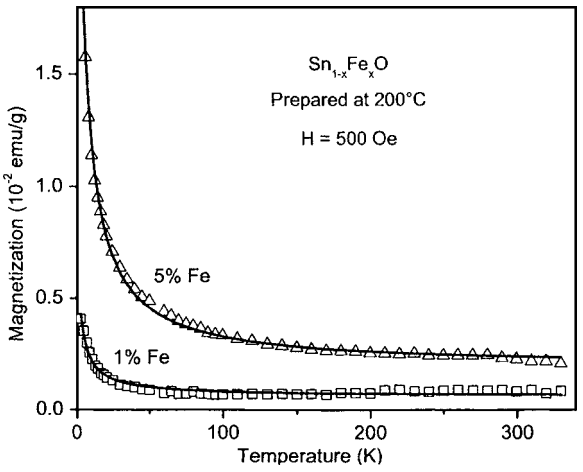

FIG. 12. M vs T data measured with $H=500$ Oe from $Sn_{1-x}Fe_xO$ samples. Solid lines are theoretical fits using the modified Curie-Weiss law.

following the modified Curie-Weiss law $\chi=\chi_0+C/(T+\theta)$, where $\chi_0=4(3)\times10^{-6}$ emu/g Oe represents weak nonparamagnetic contributions,[21] Curie constant $C=N\mu^2/3k$ (N =number of magnetic ions/g, μ=magnetic moment of the ion) and θ is the Curie-Weiss temperature. These fits showed an increase in C (as well as M_0) with x, as shown in Table II, confirming the progressive doping of Fe ions. The positive values of θ indicate AF interactions between the Fe spins as observed in other systems as well.[20,21] Both θ and T_0 decrease with x, as shown in Table II, indicating that the AF interaction decreases with increasing Fe doping. This might suggest that there are competing AF and ferromagnetic interactions as x increases. However, more detailed investigations are required to fully understand this behavior.

The pure iron oxide sample prepared under identical conditions as $Sn_{1-x}Fe_xO$ was strongly ferromagnetic [see Figs. 11(a) and 11(b)]. M versus T data, shown in Fig. 13, of this sample indicated a blocking temperature $T_B\sim21$ K, suggesting the presence of nanoscale ferromagnetic particles. These observations match very well with the XRD data showing the formation of nanoscale maghemite. This also rules out the presence of this phase in the $Sn_{1-x}Fe_xO$ samples, which are all paramagnetic for $x\leqslant0.05$.

2. $Sn_{1-x}Fe_xO_2$—*concentration dependence*

The room-temperature M versus H data of $Sn_{1-x}Fe_xO_2$ [Fig. 14(a)] showed a linear component superimposed on a

TABLE II. Variations of magnetization M_0, interaction temperature T_0, Curie constant C, and Curie-Weiss temperature θ of $Sn_{1-x}Fe_xO$ as a function of x.

	$Sn_{1-x}Fe_xO$			
Fe percentage	Magnetization M_0 (emu/g)	Interaction temperature T_0 (K)	Curie constant (10^{-4} emu K/g Oe)	Curie-Weiss temperature θ (K)
1	0.25	4.50	0.55	4.17
5	1.24	3.10	2.81	3.00

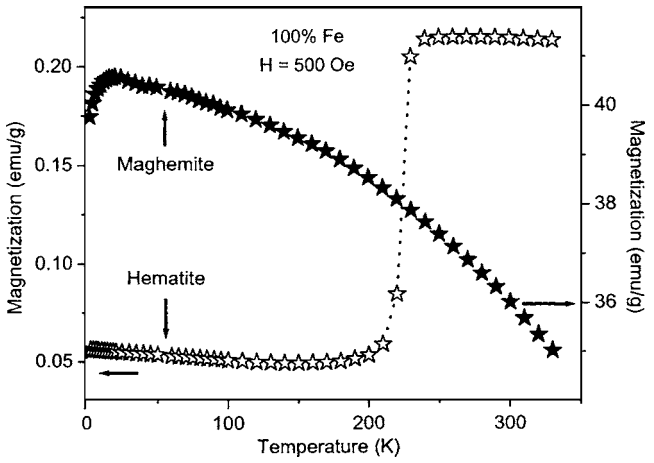

FIG. 13. M vs T data measured with $H=500$ Oe for pure iron oxide samples prepared at 200 °C (maghemite) and 600 °C (hematite).

saturating ferromagnetic-like magnetization. If this linear component χ_p is subtracted, the $M-\chi_p H$ data show saturation of M expected for a ferromagnetic phase [Fig. 14(b)]. Variations of the saturation magnetization M_s and χ_p obtained from the M versus H data as a function of x are shown in Figs. 15(a) and 15(b), respectively. At 5 K, the ferromagnetic component is overwhelmed by a paramagnetic-like component [Fig. 14(c)]. These data fit reasonably well with the modified Brillouin function, assuming $J=5/2$. This indicates that a fraction of the doped Fe is not participating in the ordered magnetic state, in excellent agreement with the Mössbauer results [Fig. 7(b)]. The exact nature of this component became more evident in the M versus T data shown in Fig. 16. This showed a paramagnetic variation described by the modified Curie-Weiss law similar to their $Sn_{1-x}Fe_xO$ counterparts (see Fig. 12), but offset by an amount χ_0 most likely due to the ferromagnetic component. It also confirms that the linear component χ_p observed in the room-temperature M versus H data [Fig. 14(a)] is also due to this paramagnetic contribution present in the sample. Interestingly, T_0 and θ [Fig. 15(c)] obtained from the M versus H and M versus T data respectively, indicate that the interaction between the disordered (paramagnetic-like) Fe^{3+} spins present in $Sn_{1-x}Fe_xO_2$ is AF in nature.

The pure hematite form of iron oxide, prepared at 600 °C following an identical synthesis procedure but with no Sn precursor, showed a weak magnetization [see Figs. 13, 14(a), and 14(c)]. The most striking characteristics of bulk hematite includes the sharp Morin transition near 263 K in the M versus T data and a spin-flop (SF) transition at H_{SF} ~67.5 kOe in the M versus H data.[12] Both of these transitions were indeed present in our pure hematite as shown in Figs. 13 and 14(c), although with reduced magnitudes presumably due to a smaller particle size of ~53 nm.[22] These transitions were clearly absent in all the $Sn_{1-x}Fe_xO_2$ samples, thus ruling out the presence of any hematite particles.

The $Sn_{1-x}Fe_xO_2$ samples showed well defined hysteresis loops at 300 K (Fig. 17) with remanence M_r and saturation magnetization M_s increasing gradually with x [see Figs. 15(a) and 15(b)]. The coercivity H_c was in the range of

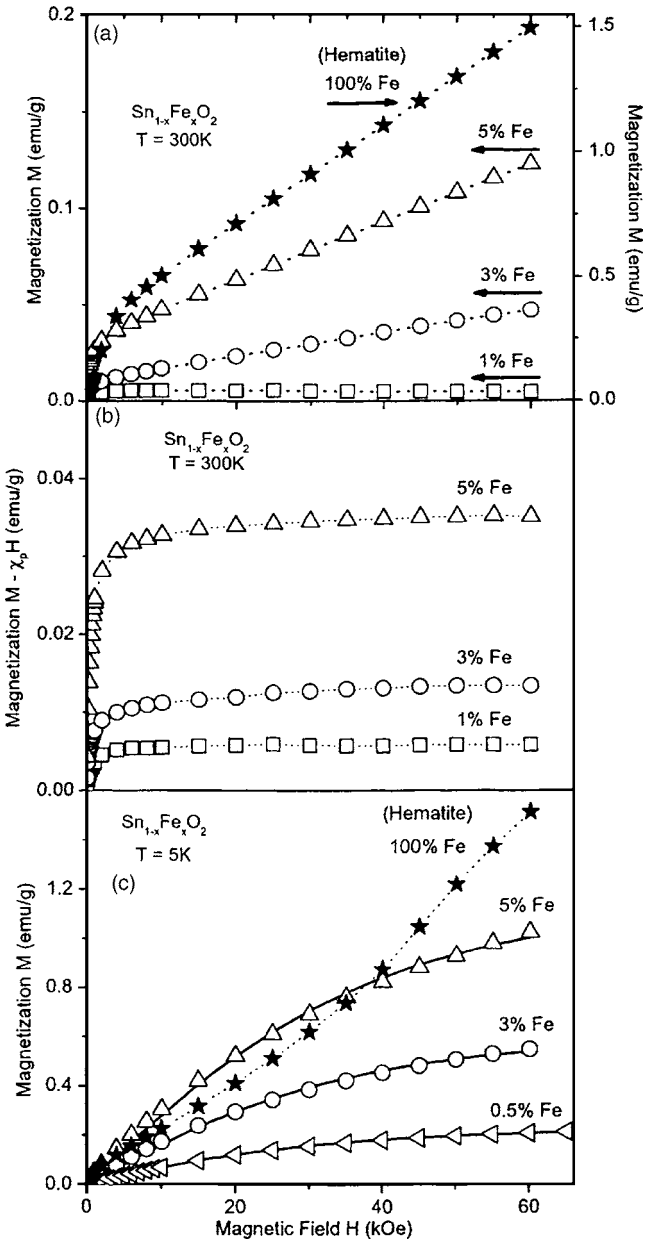

FIG. 14. (a) and (c) M vs H data of $Sn_{1-x}Fe_xO_2$ measured at 300 and 5 K, respectively. (b) $M-\chi_p H$ as a function of H for the $Sn_{1-x}Fe_xO_2$ samples measured at 300 K. Solid lines through the data points in (c) are theoretical fits using Eq. (1).

~60 Oe, which is significantly different from the value of $H_c=1844$ Oe obtained for the pure hematite sample prepared under identical conditions. The existence of a significant coercivity in $Sn_{1-x}Fe_xO_2$ samples clearly rules out their possible origin from nanoscale superparamagnetic particles of iron oxides. It is well known that when magnetic materials are prepared in nanoscale sizes, they demonstrate superparamagnetic behavior characterized by hysteresis loops with zero coercivity above their blocking temperatures.[23–25] Absence of bulk iron oxides (or nonsuperparamagnetic particles) was confirmed from Mössbauer data discussed before. Finally, a $T_C=850$ K was obtained for the 1% Fe-doped SnO_2 sample by measuring M up to 1000 K (see Fig. 18).

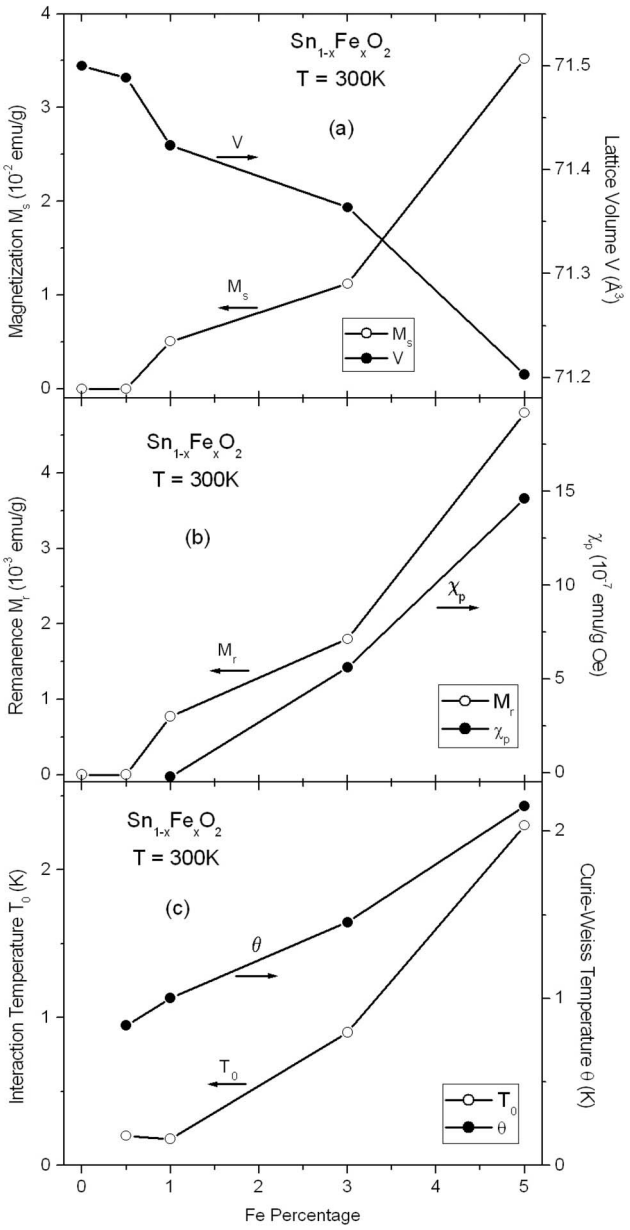

FIG. 15. Changes in (a) saturation magnetization M_s and lattice volume V, (b) remanence M_r and the linear paramagnetic component χ_p, and (c) interaction parameter T_0 and Curie-Weiss temperature θ (obtained from the paramagnetic component in Fig. 16) of the $Sn_{1-x}Fe_xO_2$ samples as a function of x.

3. $Sn_{1-x}Fe_xO_2$*—temperature dependence*

Annealing the reaction precipitate at temperatures between 350 and 900 °C produces the $Sn_{1-x}Fe_xO_2$ phase. The M versus H data measured from the $Sn_{0.95}Fe_{0.05}O_2$ prepared by annealing the same reaction precipitate at different temperatures, shown in Fig. 19, clearly shows the presence of a ferromagnetic component in samples annealed at 350, 450, and 600 °C. Only a linear variation indicating a purely paramagnetic behavior was observed in the sample prepared by annealing at 750 and 900 °C. The saturation magnetization M_s estimated after subtracting the linear paramagnetic component χ_p is plotted in Fig. 20. This clearly establishes the fact that the ferromagnetic component is stronger when prepared at lower annealing temperatures and it gradually declines with increasing preparation temperature eventually disappearing completely for preparation temperatures >600 °C, in excellent agreement with Mössbauer data discussed earlier. The remanence M_r obtained from the hysteresis loops, shown in Fig. 20, also decreases with preparation temperature.

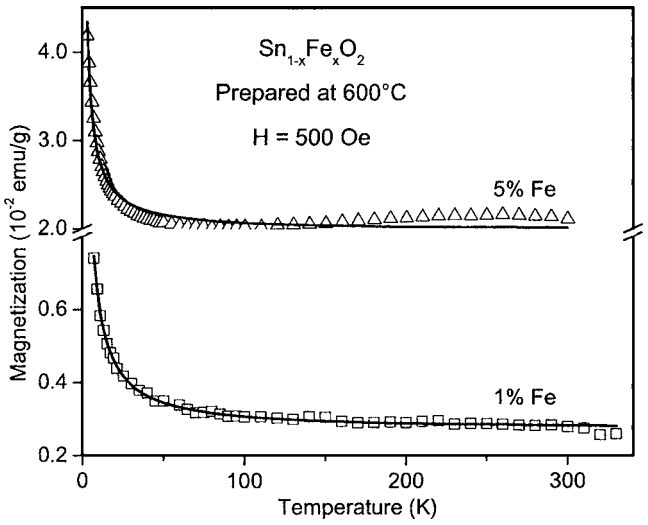

FIG. 16. M vs T data measured with $H=500$ Oe from $Sn_{1-x}Fe_xO_2$ samples. Solid lines are theoretical fits using the modified Curie-Weiss law.

IV. DISCUSSION AND CONCLUSIONS

A. Intrinsic origin of ferromagnetism

The origin of ferromagnetism in dilute magnetic semiconductor oxides has been extensively studied recently because of the possible presence of weaker secondary phases.[2] This is particularly important when the ferromagnetic component is weak. Since the sol-gel preparation of the samples and their

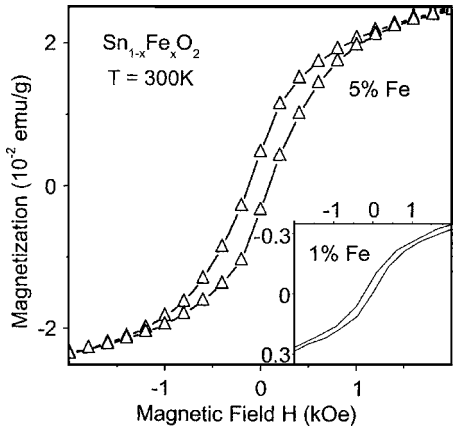

FIG. 17. Room-temperature hysteresis loops of $Sn_{1-x}Fe_xO_2$ prepared at 600 °C with $x=0.05$ (main panel) and 0.01 (inset). The lines joining the points are for visual aid.

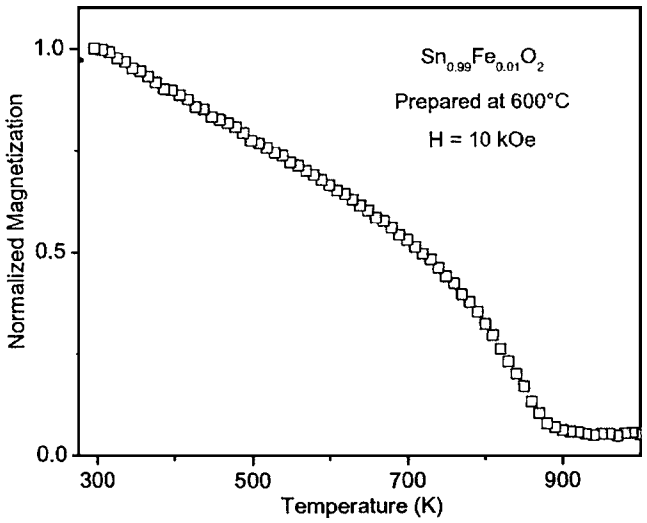

FIG. 18. Plot of the normalized sample magnetization M of a $Sn_{0.99}Fe_{0.01}O_2$ sample measured with $H=10$ kOe as a function of temperature, indicating a Curie temperature $T_C \sim 850$ K.

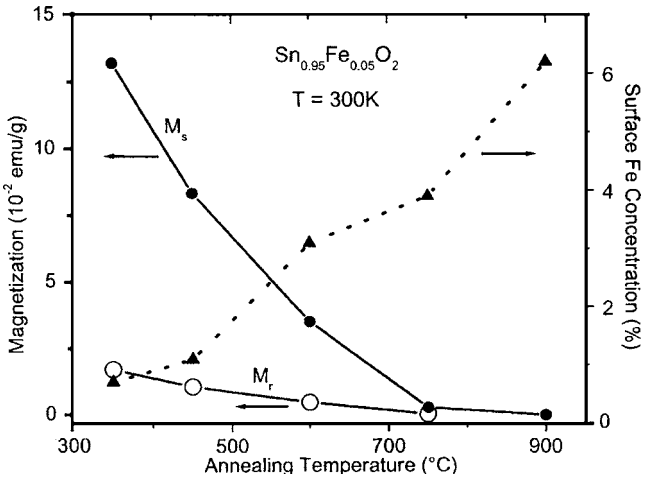

FIG. 20. Changes in the saturation magnetization M_s and remanence M_r, along with the XPS estimate of surface Fe concentration of the $Sn_{0.95}Fe_{0.05}O_2$ samples as a function of their preparation temperature.

subsequent drying and annealing processes were all conducted in air, it intrinsically eliminates the possibility of forming metallic Fe particles. However, one could argue that the ferromagnetism observed in $Sn_{1-x}Fe_xO_2$, when prepared in the 350 to 600 °C range, may be due to weak traces of maghemite or magnetite phases of iron oxide formed in the sample. The pure iron oxide samples prepared under identical synthesis conditions showed the formation of pure maghemite when prepared at 200 °C and pure hematite at 600 °C. However, no ferromagnetism was observed in the $Sn_{1-x}Fe_xO$ sample prepared by annealing the precipitate at 200 °C, which rules out the presence of any maghemite phase undetected in the XRD data. Therefore, it is unlikely that this phase will appear when the $Sn_{1-x}Fe_xO_2$ sample is prepared by annealing the same precipitate in the 350 to 600 °C range. Investigation of the phase transition of pure iron oxide samples prepared under identical conditions

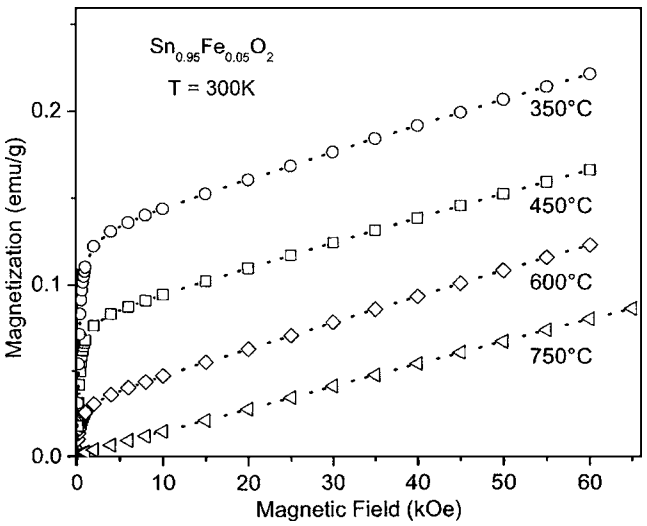

FIG. 19. M vs H data of $Sn_{0.95}Fe_{0.05}O_2$, prepared at the different temperatures indicated, measured at 300 K.

showed that the maghemite phase converted to the hematite phase when annealed at temperatures above 350 °C, in agreement with literature reports.[12] Thus, it is very unlikely to have the maghemite phase of iron oxide present in the $Sn_{1-x}Fe_xO_2$ samples prepared by annealing at temperatures $\geqslant$350 °C.

The M versus H and M versus T data obtained from $Sn_{1-x}Fe_xO_2$ samples ruled out the presence of hematite due to the absence of spin-flop and the strong Morin [see Figs. 13 and 14(c)] transitions. The hematite phase is thermally the most stable phase and it undergoes a thermal reduction to the magnetite (Fe_3O_4) phase only above 1200 °C.[12] Thus, thermodynamically, the possible formation of the magnetite phase can also be ruled out. Even if the magnetite phase is formed, the observed disappearance of ferromagnetism when prepared at temperatures above 600 °C (Fig. 20) is difficult to understand.

Furthermore, careful analysis of the samples using XRD, TEM, and selected area electron diffraction experiments ruled out the presence of any iron oxide phases in the samples. Finally, the Mössbauer data, XPS spectra, and hysteresis loop parameters obtained from the $Sn_{1-x}Fe_xO_2$ samples clearly ruled out the presence of any bulk or nanoscale magnetite, hematite, maghemite, or goethite phases of iron oxide in the samples, as discussed before.

The systematic changes in the lattice parameters, particle size and shape observed in XRD and TEM studies strongly support the progressive incorporation of Fe into the SnO_2 and SnO lattices with increasing x. The one-to-one match in the relative changes in the saturation magnetization M_s and lattice volume V [shown in Fig. 15(a)], observed in the $Sn_{1-x}Fe_xO_2$ samples, is a very strong result against any impurity being the origin of the observed ferromagnetism. It also suggests a strong structure-magnetic property relationship in these samples. The striking agreement between the estimated magnetically ordered Fe^{3+} spins ($\sim$24%) in our powder samples of $Sn_{0.95}Fe_{0.05}O_2$ and the similar estimate of ferromagnetic Fe^{3+} spins ($\sim$23%) in pulsed-laser-deposited

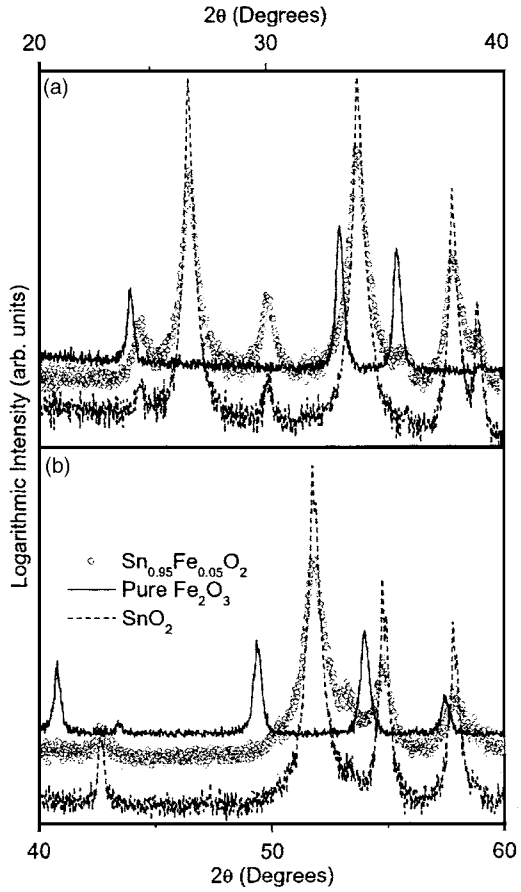

FIG. 21. (a) and (b) XRD data collected from separate angular regions for $Sn_{0.95}Fe_{0.05}O_2$ (data points), pure SnO_2 (dashed line), and pure Fe_2O_3, all prepared at 600 °C following identical synthesis procedures. The intensity is plotted on a log scale as used in Ref. 26.

thin films of $Sn_{0.95}Fe_{0.05}O_2$ by Coey *et al.*[7] further underlines the fact that the observed ferromagnetism in this system is not due to impurity iron oxide phases formed under the different preparation conditions employed.

In a recent report, Kundaliya *et al.*[26] have shown that the room-temperature ferromagnetism observed in a Mn-doped ZnO system[26,27] results from a metastable $Mn_{2-x}Zn_xO_{3-d}$ type phase formed by the diffusion of Zn into Mn oxides. In these studies, peaks due to pure and/or doped manganese oxides were clearly observed in the XRD measurements (plotted on log scale).[26] In the present work, although the saturation magnetization increases by about four times as Fe concentration increases to 5%, no indication of pure or doped iron oxides or other impurity phases is observed in the XRD measurements (shown on log scale), as illustrated in Fig. 21. In the selected area electron diffraction, XPS, or Mössbauer spectroscopy studies as well, no evidence for the presence of any such mixed phases in $Sn_{1-x}Fe_xO_2$ in the entire ranges of Fe concentration and preparation temperatures were observed. The sol-gel-based chemical synthesis employed in this work for the sample preparation is well known to provide a uniform distribution of the dopant in the host system at lower temperatures,[19] as compared to the solid state reaction used in the preparation of Mn-doped ZnO.[26,27] However, given the relatively low magnitude of the sample magnetization observed in $Sn_{1-x}Fe_xO_2$, more experimental investigations to observe anomalous Hall effect, and to understand the dependence of the ferromagnetic properties, especially T_C, on the Fe concentration, preparation temperatures, and the carrier concentration of the samples are needed to unambiguously rule out this possibility and to confirm the origin of the observed ferromagnetism to be carrier-mediated as predicted for dilute magnetic semiconductors.[28]

B. Fe concentration dependence

The systematic growth of both ferromagnetic and paramagnetic contributions in $Sn_{1-x}Fe_xO_2$ with increasing x [Figs. 15(a) and 15(b)] suggests that the ferromagnetic component is not growing at the expense of the paramagnetic Fe^{3+} ions as Fe doping increases. In a recent paper, Coey *et al.*[7] proposed a ferromagnetic exchange mechanism involving oxygen vacancies (□), which form *F*-centers with trapped electrons, for the observed ferromagnetism in Fe-doped SnO_2 thin films. Overlap of the *F*-center electron orbitals with the *d*-orbitals of the neighboring Fe^{3+} spins to form Fe^{3+}-□-Fe^{3+} groups is crucial for the proposed ferromagnetic coupling. They have argued that doped Fe^{3+} spins might also exist as isolated paramagnetic spin systems wherever the *F*-center mediated ferromagnetic coupling is not achieved due to lack of Fe^{3+} neighbors and/or oxygen vacancies. In addition, any Fe^{3+}-O^{2-}-Fe^{3+} superexchange interactions will be AF in nature. As Fe doping concentration increases, both ferromagnetic and paramagnetic/AF components will increase leading to the observed variations seen in Figs. 15(a) and 15(b).

C. Role of host system

It is well known that the *p*-type semiconducting behavior of SnO results from an excess of oxygen, whereas the existence of oxygen vacancies in SnO_2 make it an excellent *n*-type semiconductor.[8] Interestingly, the XPS data obtained for 1% and 5% Fe-doped SnO showed identical oxygen atomic percentages (see Table I), whereas the oxygen concentration decreased in $Sn_{1-x}Fe_xO_2$ with Fe concentration. The Sn—O distance of 2.057 Å in SnO_2 is lower than 2.223 Å in SnO, and this might influence the overlap of the electron orbitals. Thus, in $Sn_{1-x}Fe_xO$, Fe doping might favor the formation of antiferromagnetic Fe^{3+}-O^{2-}-Fe^{3+} groups, whereas $Sn_{1-x}Fe_xO_2$ will have a large number of ferromagnetic Fe^{3+}-□-Fe^{3+} groups because of the oxygen vacancies. This might explain the observed AF interaction in $Sn_{1-x}Fe_xO$ and ferromagnetism in $Sn_{1-x}Fe_xO_2$.

The $Sn_{1-x}Fe_xO_2$ system showed a strong structure-magnetic property relationship, illustrated in Fig. 15(a), where the increase in the saturation magnetization with Fe concentration matches with the increase in the lattice contraction. $Sn_{1-x}Fe_xO$, on the other hand, showed an expansion of the lattice with increasing Fe concentration, and here no ferromagnetism is observed. Changes in the internal or external lattice volume/pressure have been reported to produce ferromagnetism in itinerant electron metamagnets.[29–31] Thus, more investigations are required to understand the exact role

of structural changes and internal pressure differences in the observed ferromagnetism/paramagnetism of $Sn_{1-x}Fe_xO_2$/$Sn_{1-x}Fe_xO$.

D. Preparation temperature dependence

Finally, the gradual decline and subsequent disappearance of the ferromagnetic component of $Sn_{1-x}Fe_xO_2$ as the preparation temperature increases (shown in Figs. 7, 19, and 20) is another important result that needs to be discussed. Based on the observed changes in the Fe XPS peak intensity shown in Fig. 9 and the comparison of the concentrations estimated from the PIXE and XPS data listed in Table I, it was concluded that the Fe ions diffuse towards the particle surface as the preparation temperature increases, in excellent agreement with the findings of Ref. 19 (see Fig. 20). The lattice volume plotted in Fig. 4(b) shows a gradual contraction of the lattice as preparation temperature increases, presumably due to the outward diffusion and rearrangement of the doped Fe ions in the SnO_2 lattice as evidenced from the XPS data. However, above 600 °C, the lattice expands, approaching the undoped SnO_2 range, and this may be due to the expulsion of some of the doped Fe ions out of the SnO_2 lattice, as also observed by Davis *et al.*[19] using extended x-ray absorption fine structure spectroscopy. This suggests that low preparation temperatures provide a relatively uniform distribution of the Fe dopant ions in the host SnO_2 lattice, and this favors ferromagnetism. The high surface diffusion of the dopant atoms in samples annealed above 600 °C causes the gradual disappearance of this ferromagnetic behavior.

In conclusion, we have shown that powder samples of chemically synthesized $Sn_{1-x}Fe_xO_2$ with $0.005 \leqslant x \leqslant 0.05$ exhibit RTFM, while their $Sn_{1-x}Fe_xO$ counterparts show only paramagnetic behavior. The $T_C = 850$ K obtained for the 1% Fe-doped SnO_2 is among the highest T_C reported for transition-metal-doped semiconductor oxides. Preparation conditions have a strong effect on the observed magnetic properties and might act as a useful control parameter. More investigations are needed to confirm if the observed ferromagnetism is carrier-mediated.

ACKNOWLEDGMENTS

This research was supported in part by grants from Research Corporation (CC5832), Petroleum Research Fund (PRF#41870-AC10) and the DoE-EPSCoR program (DE-FG02-04ER46142). We thank Mr. S. Gomez, Quantum Design for providing the high-temperature magnetization data on one of our samples. A portion of the research described in this paper was performed at the Environmental Molecular Sciences Laboratory, a national scientific user facility sponsored by the Department of Energy's Office of Biological and Environmental Research and located at Pacific Northwest National Laboratory.

*Corresponding author. Electronic address: apunnoos@boisestate.edu

[1] G. A. Prinz, Science **282**, 1660 (1998); D. D. Awschalom and J. M. Kikkawa, Phys. Today **52**, issue 6, 33 (1999).
[2] S. A. Chambers and R. F. C. Farrow, MRS Bull. **28**, 729 (2003); W. Prellier, A. Fouchet, and B. Mercey, J. Phys.: Condens. Matter **15**, R1583 (2003); S. Picozzi, Nat. Mater. **3**, 349 (2004).
[3] S. J. Pearton *et al.*, J. Appl. Phys. **93**, 1 (2003).
[4] T. Dietl, A. Haury, and Y. M. dAubigne, Phys. Rev. B **55**, R3347 (1997) and T. Dietl, H. Ohno, and F. Matsukura, *ibid.* **63**, 195205 (2001); T. Dietl, H. Ohno, F. Matsukura, J. Cibert, and D. Ferrand, Science **287**, 1019 (2000).
[5] Y. Matsumoto *et al.*, Science **291**, 854 (2001); J. D. Bryan, S. M. Heald, S. A. Chambers, and D. R. Gamelin, J. Am. Chem. Soc. **126**, 11640 (2004).
[6] S. B. Ogale *et al.*, Phys. Rev. Lett. **91**, 077205 (2003).
[7] J. M. D. Coey, A. P. Douvalis, C. B. Fitzgerald, and M. Venkatesan, Appl. Phys. Lett. **84**, 1332 (2004).
[8] X. Q. Pan and L. Fu, J. Appl. Phys. **89**, 6048 (2001).
[9] D. G. Rancourt and J. Y. Ping, Nucl. Instrum. Methods Phys. Res. B **58**, 85 (1991).
[10] B. Lu, C. Wang, and Y. Zhang, Appl. Phys. Lett. **70**, 717 (1997).
[11] Particle size $L = 0.9\lambda/\beta\cos\theta$, where λ is the x-ray wavelength and $\beta = (B_m^2 - B_s^2)^{1/2}$ was estimated using the measured peak width B_m and the instrumental width B_s.
[12] R. Zboril, M. Mashlan, and D. Petridis, Chem. Mater. **14**, 969 (2002).
[13] S. Music *et al.*, J. Mater. Sci. Lett. **10**, 197 (1991).
[14] G. F. Goya, T. S. Berquo, and G. Fonseca, J. Appl. Phys. **94**, 3520 (2003).
[15] C. Janot, H. Gilbert, and C. Tobias, Bull. Soc. Fr. Mineral. Cristallogr. **96**, 281 (1973).
[16] J. Cashion and E. Murad, *Mössbauer Spectroscopy of Environmental Materials and their Industrial Utilization* (Kluwer Academic, New York, 2004), Chap. 5.
[17] F. van der Woude and A. J. Dekker, Phys. Status Solidi **13**, 181 (1966).
[18] N. S. McIntyre and D. G. Zetaruk, Anal. Chem. **49**, 1521 (1977).
[19] S. R. Davis, A. V. Chadwick, and J. D. Wright, J. Phys. Chem. B **107**, 9901 (1997).
[20] D. Heiman, Y. Shapira, S. Foner, B. Khazai, R. Kershaw, K. Dwight, and A. Wold, Phys. Rev. B **29**, 5634 (1984).
[21] A. Manivannan, M. S. Seehra, S. B. Majumder, and R. S. Katiyar, Appl. Phys. Lett. **83**, 111 (2003).
[22] R. D. Zysler, D. Fiorani, A. M. Testa, L. Suber, E. Agostinelli, and M. Godinho, Phys. Rev. B **68**, 212408 (2003).
[23] A. Punnoose, M. S. Seehra, J. van Tol, and L. C. Brunel, J. Magn. Magn. Mater. **288**, 168, (2005). M. S. Seehra and A. Punnoose, Solid State Commun. **128**, 299 (2003); A. Punnoose, T. Phauthavady, M. Seehra, N. Shah, and G. P. Huffman, Phys. Rev. B **69**, 054425 (2004); M. S. Seehra and A. Punnoose, *ibid.* **64**, 132410 (2001).
[24] J. T. Richardson, D. L. Yiagas, B. Turk, K. Forster, and M. V. Twigg, J. Appl. Phys. **70**, 6977 (1991).
[25] S. A. Makhlouf, F. T. Parker, F. E. Spada, and A. E. Berkowitz, J. Appl. Phys. **81**, 5561 (1997).

[26] D. C. Kundaliya, S. B. Ogale, S. E. Lofland, S. Dhar, C. J. Metting, S. R. Shinde, Z. Ma, B. Varughese, K. V. Ramanujachary, L. Salamanca-Riba, and T. Venkatesan, Nat. Mater. **3**, 709 (2004).

[27] P. Sharma, A. Gupta, K. V. Rao, F. J. Owens, R. Sharma, R. Ahuja, J. M. O. Guillen, B. Johansson, and G. A. Gehring, Nat. Mater. **2**, 673 (2003).

[28] T. Dietl, Acta Phys. Pol. A **100**, 139 (2001) and Semicond. Sci. Technol. **17**, 377 (2002). T. Dietl, H. Ohno, and F. Matsukura, Phys. Rev. B **63**, 195205 (2001). T. Dietl, H. Ohno, F. Matsukura, J. Cibert, and D. Ferrand, Science **287**, 1019 (2000).

[29] K. Yoshimura and Y. Nakamura, Solid State Commun. **56**, 767 (1985).

[30] J. G. M. Armitage, R. G. Graham, P. C. Riedi, and J. S. Abell, J. Phys.: Condens. Matter **2**, 8779 (1990).

[31] N. H. Duc and T. Goto, in *Handbook on the Physics and Chemistry of Rare Earths*, edited by K. A. Gschneidner, Jr. and L. Eyring (Elsevier, New York, 1999), Vol. 26, p. 178.